Inorganic Chemistry
Article
pubs.acs.org/IC

Outstanding Laser Damage Threshold in Li_2MnGeS_4 and Tunable Optical Nonlinearity in Diamond-Like Semiconductors

Jacilynn A. Brant,[†] Daniel J. Clark,[‡] Yong Soo Kim,[‡,§] Joon I. Jang,[‡] Ashley Weiland,[†] and Jennifer A. Aitken*,[†]

[†]Department of Chemistry and Biochemistry, Duquesne University, Pittsburgh, Pennsylvania 15282, United States
[‡]Department of Physics, Applied Physics and Astronomy, Binghamton University, Binghamton, New York 13902, United States
[§]Department of Physics and Energy Harvest-Storage Research Center, University of Ulsan, Nam-gu, Ulsan 680-749, South Korea

Supporting Information

ABSTRACT: The new Li_2MnGeS_4 and Li_2CoSnS_4 compounds result from employing a rational and simple design strategy that guides the discovery of diamond-like semiconductors (DLSs) with wide regions of optical transparency, high laser damage threshold, and efficient second-order optical nonlinearity. Single-crystal X-ray diffraction was used to solve and refine the crystal structures of Li_2MnGeS_4 and Li_2CoSnS_4, which crystallize in the noncentrosymmetric space groups *Pna*2$_1$ and *Pn*, respectively. Synchrotron X-ray powder diffraction (SXRPD) was used to assess the phase purity, and diffuse reflectance UV−vis−NIR spectroscopy was used to estimate the bandgaps of Li_2MnGeS_4 (E_g = 3.069(3) eV) and Li_2CoSnS_4 (E_g = 2.421(3) eV). In comparison with Li_2FeGeS_4, Li_2FeSnS_4, and Li_2CoSnS_4 DLSs, Li_2MnGeS_4 exhibits the widest region of optical transparency (0.60−25 μm) and phase matchability (≥1.6 μm). All four of the DLSs exhibit second-harmonic generation and are compared with the benchmark NLO material, $AgGaSe_2$. Most remarkably, Li_2MnGeS_4 does not undergo two- or three-photon absorption upon exposure to a fundamental Nd:YAG beam (λ = 1.064 μm) and exhibits a laser damage threshold > 16 GW/cm^2.

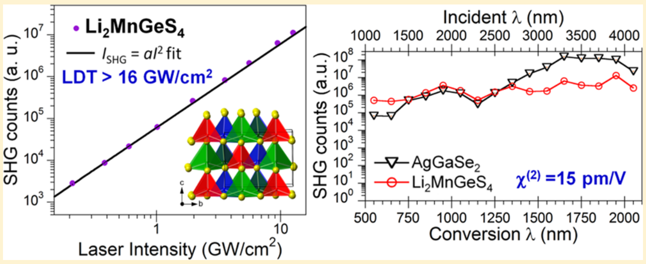

1. INTRODUCTION

Nonlinear optical (NLO) materials for the generation of infrared (IR) radiation are highly attractive for applications in military, medical, commercial, and industrial sectors. Currently, ternary diamond-like semiconductors (DLSs), such as $AgGaSe_2$, $AgGaS_2$, and $ZnGeP_2$, dominate the market for materials that exhibit second-harmonic generation (SHG) in the IR region. In addition to highly efficient second-order nonlinearity, there are a number of key characteristics (e.g., birefringence, transparency, environmental stability, laser damage threshold) that should be optimized in NLO materials for practical employment in laser systems.[1] While $AgGaSe_2$, $AgGaS_2$, and $ZnGeP_2$ demonstrate attractive second-order nonlinear optical susceptibility ($\chi^{(2)}$) values of 66, 36, and 150 pm/V, respectively,[1,2] as well as wide phase matching ranges and wide windows of optical transparency,[1,2] these ternary DLSs share the common disadvantages of difficult crystal growth, multiphoton absorption, and relatively low laser damage thresholds (LDTs) that limit practical use.[3] Although obtaining highly efficient NLO susceptibility is often the focus of research geared toward discovering new NLO materials, high $\chi^{(2)}$ values often come at the expense of diminishing critical practical properties. In fact, criteria including high LDT and noncritical phase matching may be more imperative, as noted by Peter G. Schuneman of BAE systems.[3a] Generally, materials with narrow bandgaps have low LDTs but high $\chi^{(2)}$.[4] Higher LDTs are usually accessible in semiconductors with wider bandgaps.[5] For example, $LiInS_2$[6] and $LiInSe_2$[7] exhibit relatively high LDTs; however, they are afflicted with lower $\chi^{(2)}$ values that range from 7 to 15 pm/V[8] and from 17 to 22 pm/V,[8d,9] respectively. Variability is observed in the $\chi^{(2)}$ values of $LiInS_2$ and $LiInSe_2$ due to difficulties in crystal growth that give rise to inconsistencies in the concentrations of defects. In an effort to discover new NLO materials with optimal key properties as well as concurrently high $\chi^{(2)}$ and impressive LDTs, compositional tuning in quaternary diamond-like materials was employed.

To date, the leading, mature NLO materials that are crucial for IR-radiation applications are ternary DLSs with the formula I-III-VI$_2$,[2] in which the roman numerals correspond to the number of valence electrons in the elemental state.[10] Quaternary DLSs will likely constitute the next-generation of NLO materials for the generation of long-wavelength radiation. For example, Li_2CdGeS_4 exhibits phase-matched SHG efficiency that is the highest among IR NLO materials with bandgaps larger than 3.0 eV[11] and also shows an exceptional LDT.[5] On the basis of simple guidelines, (i.e., the average

Received: December 13, 2014
Published: February 24, 2015

DOI: 10.1021/ic502981r
Inorg. Chem. 2015, 54, 2809−2819

valence electron concentration (VEC) is four, the VEC per anion is eight), all of the formulae of materials with diamond-like structures can be predicted.[10] Nine are possible for normal DLSs, in addition to defect diamond-structured materials with built-in vacancies, such as I-III-IV-□-VI$_4$ and I$_3$-IV$_2$-V-□$_2$-VI$_8$.[12] In fact, vast numbers of diamond-structured materials are reliably generated by utilizing combinations of elements that are capable of tetrahedral coordination in conjunction with satisfying the appropriate guidelines.

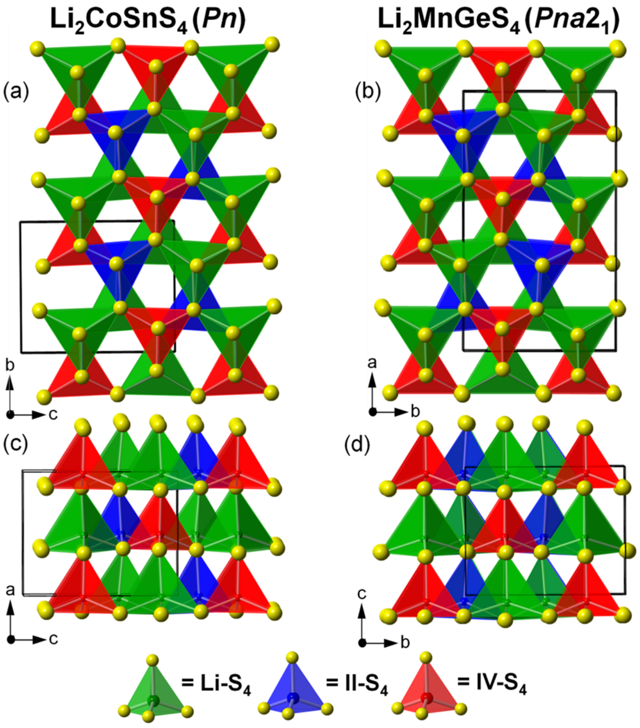

Figure 1. (a) The Li_2CoSnS_4 structure viewed down the *a* axis is compared to (b) the Li_2MnGeS_4 structure viewed down the *c* axis to accentuate the unit cell doubling that results from the arrangement of cations. (c) View of Li_2CoSnS_4 down the *b* axis shows the alignment of tetrahedra along the *a* axis. (d) View of Li_2MnGeS_4 down the *a* axis shows that tetrahedra align along the *c* axis.

The I$_2$-II-IV-VI$_4$ DLSs (Figure 1) are especially attractive for the guided discovery of new NLO materials since chalcogenides can impart wide optical transparency in the IR and terahertz (THz) ranges, a vast improvement over oxides and organics. In comparison to oxides, the greater polarizability of chalcogenides and the higher degree of covalent bonding impart large $\chi^{(2)}$. Lithium can be incorporated in this formula to widen the bandgap and optimize the LDTs. Finally, the diamond structure is inherently noncentrosymmetric, which is a prerequisite for SHG.

Here we compare the new DLSs, Li_2MnGeS_4 and Li_2CoSnS_4 (Figure 1), as well as Li_2FeGeS_4 and Li_2FeSnS_4 in the first systematic study of optical nonlinearity in quaternary DLSs, specifically those containing divalent transition metals. We report the synthesis, crystal structures, Rietveld refinements using synchrotron X-ray powder diffraction (SXRPD) data, and optical bandgaps of the new Li_2MnGeS_4 and Li_2CoSnS_4. The phase matchability of the SHG is reported for Li_2FeGeS_4, Li_2CoSnS_4, and Li_2MnGeS_4. The optical transparency ranges and the broad-band wavelength dependence of SHG are reported for all four of the quaternary DLSs. Finally, an outstanding LDT of the most promising NLO compound, Li_2MnGeS_4, is reported.

2. EXPERIMENTAL SECTION

2.1. Synthesis. Li_2MnGeS_4 was obtained by grinding in an agate mortar and pestle stoichiometric amounts of Mn chips (0.8−3 mm, 99.99%, Cerac), Ge pieces (ground using a diamonite mortar and pestle, 99.999%, Strem), and S (sublimed powder, 99.5%, Fisher Scientific) plus a 20% excess of Li_2S (∼200 mesh, 99.9%, Cerac) that can act as a molten Li_2S_x flux at elevated temperatures. The mixture was placed into a graphite crucible inside a 12 mm o.d. fused-silica tube that was sealed under vacuum, ∼10^{-4} mbar. The reaction vessel was heated at 700 °C for 144 h, slowly cooled to 650 °C in 50 h, and then allowed to cool to room temperature naturally. The reaction vessel was opened under ambient conditions, and the product was rinsed with methanol to remove the excess Li_2S_x flux. A pale-orange polycrystalline powder was observed using an optical microscope.

Li_2CoSnS_4 was prepared in a similar manner, except the reaction contained Co (∼100 mesh, 99.99%, Strem) and Sn (∼200 mesh, 99.99%, Cerac), and was heated at 650 °C for 144 h and cooled to 550 °C in 100 h. The resulting polycrystalline product was bright green.

The synthesis of microcrystalline $AgGaS_2$(MC) was adapted from the method reported by Zhao et al.[13] MC is used to denote a microcrystalline sample that was prepared using conventional high-temperature, solid-state synthesis. The starting materials, stoichiometric amounts of Ag (∼325 mesh, 99.99%, Cerac), Ga (99.99%, Strem), and S, were prepared in the same manner as in the synthesis of Li_2MnGeS_4 and Li_2CoSnS_4. However, the reaction vessel was heated at 300 °C for 1.2 h, heated to 400 °C at a rate of 50 °C/h and held at 400 °C for 1.2 h, then heated to 940 °C at a rate of 50 °C/h, held at 940 °C for 72 h, and then radiatively cooled to room temperature. The reaction yielded a yellow product [$AgGaS_2$(MC)] that was used to assess LDT.

$AgGaSe_2$(MC) was prepared using a similar high-temperature, solid-state synthesis[5] and used as a reference for SHG measurements. The $AgGaSe_2$(OQ) and $AgGaS_2$(OQ) references were obtained by grinding optical-quality single crystals provided by Gooch and Housego.

2.2. Single-Crystal X-ray Diffraction. Single-crystal X-ray diffraction data were collected using a Bruker SMART Apex 2 CCD single-crystal X-ray diffractometer employing graphite-monochromatized Mo K$_\alpha$ radiation (λ = 0.71073 Å) with a tube power of 50 kV and 30 mA.

Data were collected for a pale orange block-like crystal of Li_2MnGeS_4 and a bright green block-like crystal of Li_2CoSnS_4 for 20 s per frame and 30 s per frame, respectively, at room temperature. Over a hemisphere of data were collected in 0.3° steps in ω and ϕ. Data were integrated using SAINT, and the absorption correction was applied using SADABS.[14] Using XPREP, the space group was determined and files for SHELXTL were created.[15]

For Li_2MnGeS_4, two space groups were initially considered based on systematic absences: *Pnma* (No. 62) and *Pna*2$_1$ (No. 33). In agreement with the noncentrosymmetric nature of diamond-like structures, the space group *Pna*2$_1$ was used to solve the structure of Li_2MnGeS_4. For Li_2CoSnS_4, three space groups were initially considered based on systematic absences, *P*2/*n* (No. 13), *P*2$_1$/*n* (No. 14), and *Pn* (No. 7). The noncentrosymmetric space group *Pn* was chosen since diamond-like structures are inherently noncentrosymmetric.

The crystal structures of Li_2MnGeS_4 and Li_2CoSnS_4 were solved and refined using the SHELXTL-PC software package.[16] The final refinement statistics and crystallographic details are displayed in Table 1. For the structure of Li_2MnGeS_4, all atoms were refined anisotropically, while Li(1) and Li(2) in the Li_2CoSnS_4 structure were refined isotropically. Atomic coordinates as well as selected bond distances and angles are displayed in Tables S1−S6, Supporting Information. All crystal structure figures were generated using CrystalMaker.

Table 1. Crystallographic Data and Experimental Details[a]

formula	Li_2MnGeS_4	Li_2CoSnS_4
size (mm)	0.20× 0.08 × 0.05	0.05 × 0.05 × 0.03
temp. (K)	298	298
space group	$Pna2_1$	Pn
a (Å)	13.3546(2)	6.3432(2)
b (Å)	7.8871(1)	6.7184(2)
c (Å)	6.2806(1)	7.9404(3)
β (deg)	90	89.988(2)
vol. (Å^3), Z	661.53(2), 4	338.39(2), 2
density (g cm^{-3})	2.708	3.139
reflns collected/unique	7045/1144	3653/1464
data/restraints/params	1144/1/75	1464/2/64
completeness to θ = 27.11°	100%	99.7%
Flack parameter	0.022(7)	0.15(3)
goodness of fit	0.83	1.03
R indices [$I > 2\sigma(I)$]	R_1 = 0.0097, wR_2 = 0.0252	R_1 = 0.0250, wR_2 = 0.0477
R indices (all data)	R_1 = 0.0109, wR_2 = 0.0273	R_1 = 0.0315, wR_2 = 0.0494
highest peak, deepest hole (e/Å^3)	0.31, −0.20	0.75, −0.54

[a] Refinement of F^2 was made against all reflections. $R_1 = (\Sigma||F_o| - |F_c||)/(\Sigma|F_o|)$. $wR_2 = \sqrt{(\Sigma[w(F_o{}^2 - F_c{}^2)^2]/\Sigma[w(F_o{}^2)^2])}$. $w = 1/(\sigma^2(F_o{}^2) + (aF_o)^2 + bP)$, $P = [2F_c{}^2 + \mathrm{Max}(F_o{}^2,0)]/3$.

2.3. High-Resolution Synchrotron X-ray Powder Diffraction (SXRPD) and Rietveld Refinement. Room temperature SXRPD data were collected at the Advanced Photon Source, Argonne National Laboratory at the 11-BM line, as described in the Supporting Information.

Rietveld refinements were conducted using the General Structure Analysis System (GSAS) with EXPGUI.[17] The crystal structures of Li_2MnGeS_4 and Li_2CoSnS_4 that were obtained using single-crystal X-ray diffraction and reported herein were used as starting models. A shifted Chebyshev polynomial was used for background correction, and peak shapes were modeled using Lorentzian isotropic crystallite size broadening (LX) and Lorentzian isotropic strain broadening (LY) terms within the type-3 profile function. Lattice parameters, atomic coordinates, and isotropic displacement parameters were refined. The structure parameters obtained from Rietveld refinement, such as unit cell parameters, atomic coordinates, atomic displacement parameters, and bond lengths and angles shown in Tables S7−S14, Supporting Information, were in good agreement with those obtained using single-crystal X-ray diffraction.

2.4. Inductively Coupled Plasma Optical Emission Spectroscopy (ICP-OES). Inductively coupled plasma optical emission spectroscopy (ICP-OES) was used for quantitative analysis of Li, Co, Mn, Ge, Sn, and S as described elsewhere.[18] Relative standard deviations are calculated by analyzing the historical performance of digested control samples.

2.5. Optical Diffuse Reflectance UV−vis−NIR Spectroscopy. Optical diffuse reflectance spectra for Li_2MnGeS_4 and Li_2CoSnS_4 were collected using a Cary 5000 UV/vis/NIR spectrometer equipped with a Harrick Praying Mantis diffuse reflectance accessory as described previously.[19]

2.6. Attenuated Total Reflectance (ATR) IR Spectroscopy. Infrared spectra for Li_2FeGeS_4, Li_2FeSnS_4, Li_2MnGeS_4, and Li_2CoSnS_4 were collected using a Thermo Nicolet 380 FT-IR spectrometer equipped with an attenuated total reflectance (ATR) accessory. The IR spectra are comprised of 64 scans, from 400 to 4000 cm^{-1}. The OMNIC software was used for data collection and analysis. The FT-IR system uses a diamond crystal in optical contact with the sample. Thus, the depth of penetration into the sample is ∼2 μm, which is near the lower limit of the particle sizes for the samples. Therefore, the effect of thickness dependence on the intensity of the measured spectrum is negligible.[20]

2.7. Second-Harmonic Generation (SHG). Samples were prepared by sieving the polycrystalline powders into discrete particle-size ranges with diameters (d) of 2−20, 20−45, 45−63, 63−75, 75−90, 90−106, 106−125, and 125−150 μm. For the Li_2CoSnS_4 and Li_2FeSnS_4 samples, only particle sizes up to 90 and 63 μm, respectively, were accessible using the synthetic conditions described herein and by Brant et al.[19] Each sample was placed into a fused-silica tube that was flame sealed under vacuum to prevent air and moisture exposure upon laser irradiation, although the compounds are stable under ambient conditions. Each tube was mounted on a Z-scan translation stage via a homemade sample holder. Powdered $AgGaSe_2$(MC) and $AgGaSe_2$(OQ)[5] were used as reference materials.

The SHG responses were measured at room temperature, as a function of both broad-band wavelength and particle size. Coherent light with a wavelength of 1.064 μm was initially produced using an EKSPLA PL-2250 series diode-pumped Nd:YAG laser with a pulse width of 30 ps and a repetition rate of 50 Hz to generate tunable pulses. The Nd:YAG laser pumped an EKSPLA Harmonics Unit (HU) H400, in which the input beam was frequency tripled by a sum frequency generation scheme. The beam then entered an EKSPLA PG403-SH-DFG Optical Parametric Oscillator (OPO) composed of four main parts: (i) a double-pass parametric generator, (ii) a single-pass parametric amplifier, (iii) a second-harmonic generator (SH), and (iv) a difference frequency generation (DFG) scheme. Output of the OPO was used for measurements with incident wavelengths (λ) ranging from 1.1 to 2.1 μm in 0.2 μm increments, while outputs from the DFG scheme provided λ ranging from 2.301 to 4.1 μm in 0.2 μm increments. Thus, the experimental spectral range of the wavelength-dependent SHG wavelength (λ_{SHG}) was 0.55−2.05 μm with steps of 0.1 μm.

The incident pulse energy was tuned to 17 μJ before being mildly focused onto samples with a spot size diameter of ∼0.5 mm using a CaF_2 convex lens. The beam spot size was determined to ensure that (i) the SHG signals from powders of random orientations were efficiently generated and properly averaged and (ii) the change in the spot size was minimized as the fundamental wavelength, λ, was varied over a broad-band range since the beam waist, w_0, at the focus undergoes a significant λ-dependent variation via $w_0 = (\lambda/\pi)(f/\sigma)$, where f and σ are the focal length and the Gaussian width of the incident beam, respectively.[21] The NLO signals from the samples were collected using a reflection geometry by a fiber optic bundle, which was coupled to a selective-grating (1800, 600, and 300 grooves/mm) spectrometer equipped with a charge-coupled device camera (Synapse) as well as an extended InGaAs (Symphony) detector. The relative SHG signals were spectrally resolved and precisely calibrated using the exposure times as well as the known and measured efficiencies of all optical components. SHG signals from other optical components and surface-induced effects were negligible. Any thermal load on the samples by the laser pulse photon energy tuned below the bandgap was negligible due to its slow repetition rate of 50 Hz.

In the λ-dependent SHG data for all samples, a dip near λ_{SHG} = 0.95−1.05 μm arises from linear absorption of the incident beam by the container (quartz tubes); however, this does not interfere with the estimation of $\chi^{(2)}$. The size-dependent SHG responses were used to indicate phase-matchability ranges for each compound, with the exception of Li_2FeSnS_4.

2.8. Laser Damage Threshold (LDT). SHG responses were measured at room temperature as a function of laser intensity up to 16 GW/cm^2 on the Li_2MnGeS_4 sample as well as the reference samples $AgGaSe_2$(MC),[5,22] $AgGaS_2$(MC), and $AgGaS_2$(OQ). The commonly used Nd:YAG line of 1.064 μm was used as the incident radiation. It should be noted that the LDT of a material is significantly dependent on the pulse width, and here all of the LDTs are presented for temporal pulse widths of 30 ps.

3. RESULTS AND DISCUSSION

3.1. Crystal Structures. The new compounds, Li_2MnGeS_4 and Li_2CoSnS_4, have crystal structures that are both related to hexagonal diamond (Figure 2). Li_2MnGeS_4 adopts the lithium

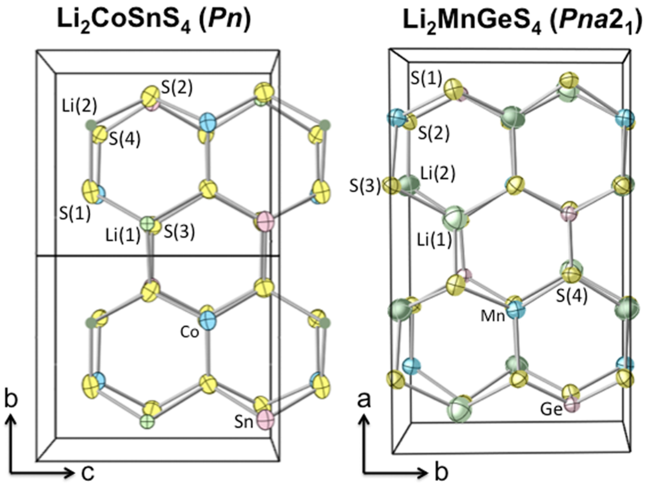

Figure 2. Oak Ridge thermal ellipsoid plots (ORTEPs) for Li_2CoSnS_4 (left) and Li_2MnGeS_4 (right). Thermal ellipsoids are drawn at 90% probability except for Li(2), which is shown as a sphere for clarity purposes, U_{iso} = 0.11(1) Å.

cobalt (II) silicate structure type ($Pna2_1$),[23] a rare structure type for quaternary DLSs with the only other example being Ag_2CdGeS_4.[24] The IV-VI framework in the lithium cobalt (II) silicate structure is comparable to that of the other diamond-like structure types derived from hexagonal diamond; however, the different patterns of I and II cations yield a doubling along one of the crystallographic axes (Figures 1 and 2). The structure of Li_2MnGeS_4 is comprised of sulfide anions packed into a hexagonal array, with lithium, manganese, and germanium occupying one-half of the tetrahedral holes. The local charge is balanced in this structure, as well as in the Li_2CoSnS_4 structure reported here, as each sulfide anion is coordinated by two monovalent ions, one divalent ion, and one tetravalent ion. Each cation in Li_2MnGeS_4 coordinates to four tetrahedral sulfide anions, and all of the tetrahedra align along the *c* axis, rendering the structure noncentrosymmetric, see Figure 1. The refined structure model that resulted from Rietveld refinement using SXRPD data is in agreement with that obtained using single-crystal X-ray diffraction (see Tables S1−S4, Supporting Information, for structural details). The related diamond-like structure types that arise from variations in the global arrangement of cations, i.e., wurtz-stannite[25] and wurtz-kesterite,[25a,26] were not evident in the SXRPD data, indicating that no other polymorphs were present in this sample.

The Li_2CoSnS_4 DLS has the wurtz-kesterite structure,[25a,26] which crystallizes in the monoclinic space group *Pn*. The majority of quaternary DLSs adopt the stannite structure,[18] while the wurtz-kesterite structure is relatively rare. This structure is adopted by Li_2FeGeS_4 and Li_2FeSnS_4[18] as well as Ag_2FeSiS_4,[18] Ag_2ZnSiS_4,[27] and Li_2ZnSnS_4.[28] The noncentrosymmetric structure of Li_2CoSnS_4 is comprised of tetrahedra that align along the *a* axis, as shown in Figure 1. It is noteworthy that the β angle in the monoclinic structure of Li_2CoSnS_4 is 89.988(2)°, and the unit cell is similar to those in the quaternary DLSs that crystallize in the orthorhombic space group $Pmn2_1$, such as Li_2CdGeS_4 and Li_2CdSnS_4.[29] The lower symmetry of the monoclinic structure, in comparison to the orthorhombic structure, does not arise from lattice distortions but rather from the cation ordering arrangement. Although the unit cell parameters are comparable to those found in orthorhombic structures, this structure simply cannot be described by *mmm* symmetry. In support of this result, the crystal structure could not be successfully solved and refined from the single-crystal X-ray diffraction data using the $Pmn2_1$ or the $Pna2_1$ space group. Attempting to add the wurtz-stannite or lithium cobalt (II) silicate structure types to the Rietveld refinement using SXRPD data yielded extreme divergence.

ICP-OES was used to confirm the presence of the appropriate ratio of the elements within the crystals. Accordingly, stoichiometries of $Li_{2.1(2)}Mn_{1.09(8)}Ge_{1.0(1)}S_{3.8(4)}$ and $Li_{1.8(2)}Co_{1.3(2)}Sn_{0.92(4)}S_{3.9(4)}$ were observed.

3.2. Synchrotron X-ray Powder Diffraction (SXRPD) and Rietveld Refinements. Using SXRPD data, Rietveld refinements indicate that the Li_2MnGeS_4 sample has been synthesized with >97% phase purity (Figure 3). All of the peaks observed in the laboratory-grade X-ray powder diffraction pattern could be indexed to the Li_2MnGeS_4 phase, and no other peaks are observed. However, high-resolution, high-intensity synchrotron X-ray diffraction data reveal the presence of two impurities in small quantities. The low-intensity impurity peaks were indexed using DICVOL[30] to two orthorhombic phases that were later identified as S_8[31] and Mn_2GeS_4.[32] All of the peaks in the pattern are indexed, and excellent agreement factors of χ^2 = 2.259, wR_p = 0.0836, and R_p = 0.0696 were achieved. The impurity phases were quantified as 1.74(3) wt % of S_8 and 1.09(3) wt % of Mn_2GeS_4. Neither S_8 nor Mn_2GeS_4 artificially enhance the SHG but rather could detract from it since they are centrosymmetric.

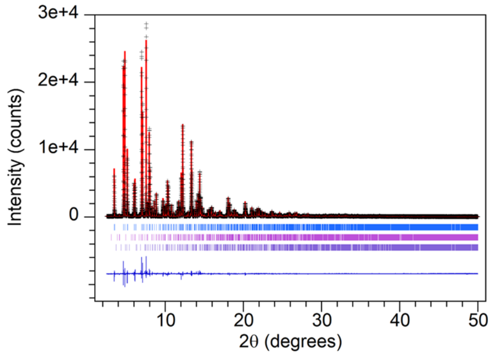

Figure 3. Rietveld refinement of the Li_2MnGeS_4 structure model using SXRPD data (λ = 0.4138310 Å) plotted with plus signs (+) representing collected data, overlapped by the pattern calculated from the model (line). Expected Bragg reflections for the Li_2MnGeS_4, S_8, and Mn_2GeS_4 phases are displayed from top to bottom, respectively, with tick marks (|). The difference between the observed data and the calculated pattern is shown at the bottom of the plot.

For the Li_2CoSnS_4 sample, Rietveld refinement (χ^2 = 2.730, wR_p = 0.1078, R_p = 0.0839) using SXRPD data reveals the presence of 10.9(6) wt % of CoS (langisite)[33] that crystallizes in the centrosymmetric space group $P6_3/mmc$, as shown in Figure 4. A few extra, low-intensity peaks, with intensities up to ~1.5% of the highest intensity peak in the pattern, could not be indexed.

The analysis of the SXRPD data for Li_2FeGeS_4 and Li_2FeSnS_4 indicates that both samples have a high degree of phase purity, as previously reported.[19]

3.3. Optical Bandgaps. The bandgaps were estimated from optical diffuse reflectance UV−vis−NIR spectra. First, the Urbach tail was fit using eq 1, where *A* is a constant, E_g is the bandgap, and E_u is the Urbach energy.[34]

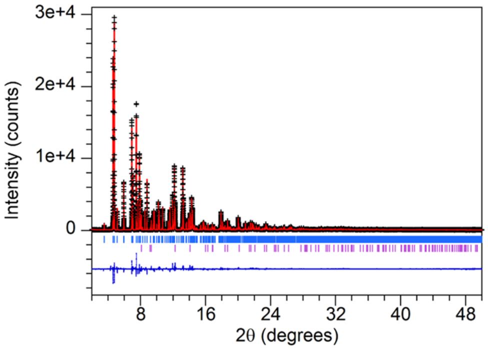

Figure 4. Rietveld refinement of the Li_2CoSnS_4 structure model using SXRPD data (λ = 0.4137330 Å) plotted with plus signs (+) representing collected data, overlapped by the pattern calculated from the model (line). Expected Bragg reflections for the Li_2CoSnS_4 and CoS phases are displayed from top to bottom, respectively, with tick marks (|). The difference between the observed data and the calculated pattern is shown at the bottom of the plot.

$$f(E) = A \exp[(E - E_g)/E_u] \tag{1}$$

A broadened distribution of electronic states around the bandgap causes Urbach tailing.[34] The Urbach tail region was excluded from the region of the absorption edge that was considered for determination of the bandgap. Next, the data were plotted as $(\alpha E)^2$ vs E and $(\alpha E)^{1/2}$ vs E to emphasize the direct or indirect nature of the optical transitions.[34,44] The absorption edges for direct-gap semiconductors exhibit wider regions of linearity in the $(\alpha E)^2$ vs E plot and can be fit with eq 2, while the absorption edges for indirect-gap semiconductors show wider linearity in the $(\alpha E)^{1/2}$ vs E plot and can be fit with eq 3.

$$\alpha(E) = A(E - E_g)^2/E \tag{2}$$

$$\alpha(E) = A(E - E_g)^{1/2}/E \tag{3}$$

As shown on the left of Figure 5, the absorption edge for Li_2MnGeS_4 exhibits Urbach tailing up to an energy of 3.33 eV. Above 3.33 eV, the $(\alpha E)^2$ vs E plot has a wider region of linearity than the $(\alpha E)^{1/2}$ vs E plot, as highlighted in black. Thus, Li_2MnGeS_4 is assigned as a direct-gap semiconductor, and the absorption edge is best fit with eq 2, yielding a bandgap of 3.069(3) eV.

The spectrum of Li_2CoSnS_4 contains an Urbach tail up to 2.55 eV. Above this energy, the $(\alpha E)^2$ vs E plot has a wider linear region than the $(\alpha E)^{1/2}$ vs E plot; thus, the absorption edge for Li_2CoSnS_4 is also fit with eq 2. The x intercept of the fit corresponds to a direct bandgap of 2.421(3) eV. As reported by Brant et al., Li_2FeGeS_4 and Li_2FeSnS_4 exhibit indirect and direct bandgaps of 1.423(3) and 1.860(2) eV, respectively.[19]

According to previous electronic structure calculations,[5] the bandgap of the similar diamond-like Li_2CdGeS_4 is mainly dictated by charge transfer from S-3p orbitals to Ge-4s orbitals. The states at the valence-band maximum (VB_{max}) are dominated by S-3p orbitals with minor contributions from the Cd-5p orbitals, while the states at the conduction-band

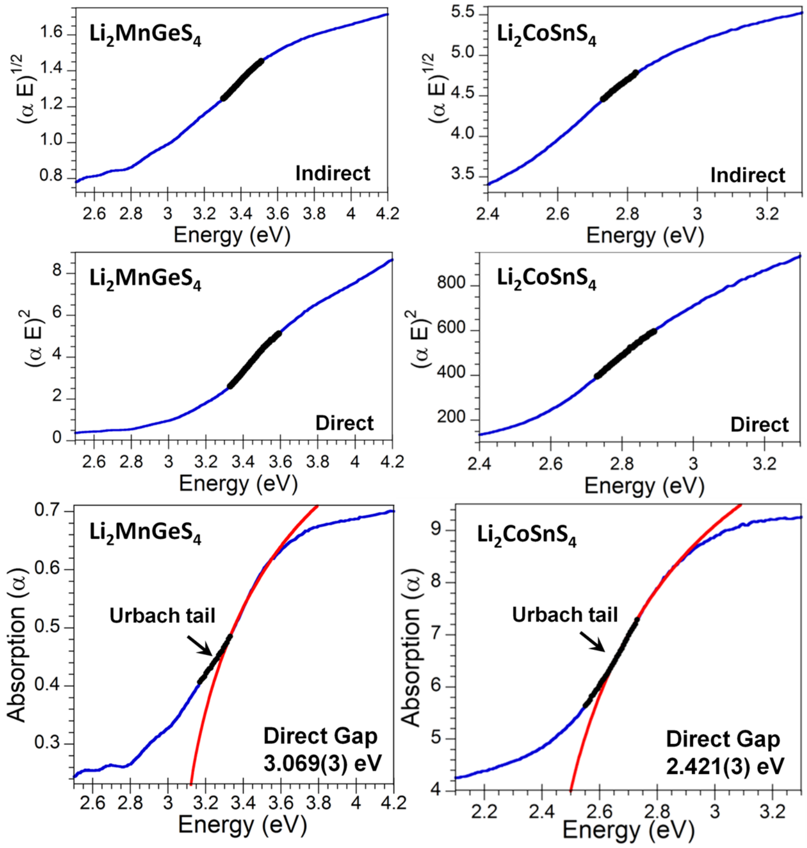

Figure 5. (Top and middle) Diffuse reflectance UV−vis−NIR spectra for Li_2MnGeS_4 (left) and Li_2CoSnS_4 (right) are scaled to emphasize direct and indirect optical transitions. (Bottom) Both spectra are fit (red) using Tauc's function for direct semiconductors, while the Urbach tail regions are excluded from the absorption edge for bandgap determination.

minimum (CB_{min}) arise from Ge-4s and S-3p orbitals. The contributions from the orbitals of Li atoms are mostly spread throughout the conduction-band states and provide minimal contribution to the valence-band states; thus, lithium acts as an electron donor, and the bandgap is widened in comparison to Cu- and Ag-based analogues whose valence-band maxima are dominated by coinage metal-d states.[11,27] It has been proposed that changing Cd to another II ion in the Li_2-II-GeS_4 formula can allow properties to be tuned, while a bandgap similar to Li_2CdGeS_4 can be maintained.[11]

Just as in the examples of β-$NaFeO_2$-type Li-III-S_2[35a] and Li-III-Se_2[35b] and chalcopyrite-like Li-III-Te_2,[36] it is expected that the electronic structures are more dependent on composition rather than the specific diamond-like crystal structure.[11] In Li_2-II-IV-S_4, where II = Fe, Co, the bandgaps are substantially decreased (~0.8–1.3 eV) in comparison to Li_2CdGeS_4, which may be accredited to much more prominent contributions from Fe/Co-4s and Fe/Co-4p orbitals to states at the VB_{max} and CB_{min}. Further, Sn-5p orbitals are expected to provide dominant character to the CB_{min} in Li_2FeSnS_4, similar to that shown by the partial density of states for Li_2CdSnS_4[37] and Cu_2CdSnS_4.[38]

Changing the II ion to Mn in Li_2-II-GeS4 indeed yields a bandgap that is comparable to that of Li_2CdGeS_4. In Li_2MnGeS_4, the VB_{max} and CB_{min} are likely dominated by contributions from S-3p and Ge-4s orbitals. Just as minor Cd-5p character is observed in the vicinity of the Fermi level for Li_2CdGeS_4, small contributions from the Mn-4s and Mn-4p orbitals likely give rise to the small variance (<0.1 eV) in bandgap.

3.4. Optical Transparency.

Diffuse reflectance UV–vis–NIR spectroscopy was used in conjunction with attenuated total reflectance (ATR) IR spectroscopy to assess the windows of optical clarity for Li_2MnGeS_4, Li_2CoSnS_4, Li_2FeGeS_4, and Li_2FeSnS_4. All of these DLSs exhibit optical transparency into the far IR. In fact, their transparency seems to extend beyond the detection limit of FT-IR (25 μm), indicating great potential as a THz generator.

As shown in Figure 6, Li_2FeGeS_4 absorbs radiation in the visible region (deep red) due to the bandgap (0.871 μm, 11 500 cm^{-1}) and the transparency region has a lower limit of ~3 μm (3300 cm^{-1}) that arises due to ^5E (^5D) → $^5T_2$ (^5D) transitions that are characteristic of Fe^{2+} $3d^6$ ions.[39] Similarly, Li_2FeSnS_4 exhibits bandgap absorption (0.667 μm, 15 000 cm^{-1}) in the visible region (red) as well as the ^5E → $^5T_2$ transition.[39] Thus, Li_2FeGeS_4 and Li_2FeSnS_4 have windows of optical transparency > 80% from ~3.0 to 25 μm.

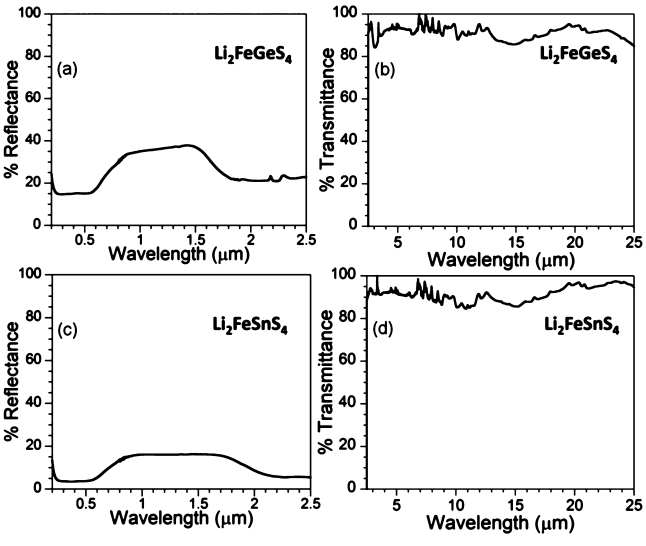

Figure 6. Diffuse reflectance UV–vis–NIR spectra (a and c) and ATR IR spectra (b and d) of Li_2FeGeS_4 and Li_2FeSnS_4, respectively.

The Li_2CoSnS_4 sample exhibits band-gap (0.512 μm, 19 500 cm^{-1}) absorption in the visible region (green), as well as significant absorption edges at ~0.80 (13 000 cm^{-1}), ~1.1 (9100 cm^{-1}), ~2.1 (4800 cm^{-1}), and ~3.5 μm (2900 cm^{-1}), as shown in Figure 7. While tetrahedral Co^{2+} ($3d^7$) ions give rise to three intense absorption bands that are generally observed at approximately 0.67, 0.71 and 1.5 μm,[39] the absorption observed here is expectedly influenced by the presence of Co-containing impurities, including the CoS that was observed using SXRPD. According to these results, this sample exhibits >65% transparency in the region of ~4.0–25 μm.

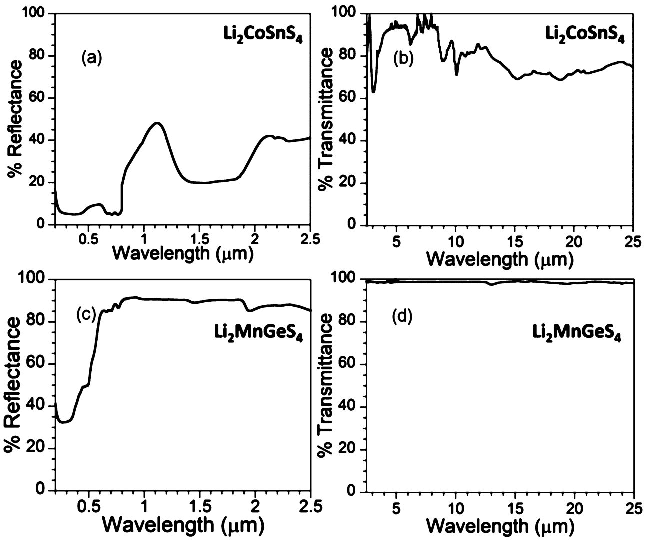

Figure 7. Diffuse reflectance UV–vis–NIR spectra (a and c) and ATR IR spectra (b and d) of Li_2CoSnS_4 and Li_2MnGeS_4, respectively.

Li_2MnGeS_4 has the widest bandgap (0.404 μm, 24 800 cm^{-1}) of the DLSs presented here. Mn^{2+} ($3d^5$) ions exhibit characteristic absorption bands ranging from 0.39 to 0.54 μm (25 300–15 006 cm^{-1}).[39] The optical clarity window with transparency > 80% is 0.60–25 μm for Li_2MnGeS_4, which is more impressive than the DLS Li_2CdGeS_4 in terms of the level of transparency approaching 100% at 25 μm and longer.[5] This wide region of transparency is broader than the clarity windows of new chalcogenides with second-order nonlinearity, such as $K_2P_2Se_6$ (0.596–19.8 μm)[40] and $Na_2Ge_2Se_5$ (0.521–18.2 μm),[41] as well as the closely related DLS, Cu_2CdSnS_4 (1.37–25 μm, T > 60%).[38] Most noteworthy, the optical transparency region obtained here for Li_2MnGeS_4 is wider than those of the ternary DLSs, $AgGaS_2$ (0.47–13 μm),[42] $AgGaSe_2$ (0.71–19 μm),[43] $ZnGeP_2$ (0.74–12 μm),[44] and $LiInS_2$ (0.34–13.2 μm), albeit at "0" level, which is assessed by measurements using laser calorimetry on single-crystal samples.[6]

3.5. Second-Harmonic Generation (SHG) and Phase Matchability.

SHG was assessed as a function of broad-band wavelength dependence for all of the compounds, and particle-size dependence of SHG was assessed for Li_2FeGeS_4,

Li_2CoSnS_4, and Li_2MnGeS_4 to determine the wavelengths at which these DLSs are phase matchable. Particle-size dependence of Li_2FeSnS_4 was not assessed since the sample only contained particles with diameters less than 65 μm. A positive trend in SHG response with increasing particle size indicates that a material is phase matchable at the applied wavelength.[45] As shown in Figures S2−S4, Supporting Information, particle-size-dependent SHG responses were assessed at fundamental λ ranging from 1.1 to 1.8 μm for Li_2FeGeS_4, 1.1 to 2.1 μm for Li_2CoSnS_4, and 1.1 to 3.3 μm for Li_2MnGeS_4.

Li_2FeGeS_4 exhibits an SHG response up to λ = 1.8 μm, which corresponds to an SHG conversion wavelength (λ_{SHG}) of 0.9 μm. Poor SHG efficiency for $\lambda > 1.8$ μm is a result of linear absorption of the SHG beam as well as the fundamental beam, which is evidenced by the UV−vis−NIR spectrum in Figure 6. Since the sample with the smallest particle-size range exhibits the highest SHG response for all of the measured λ, Li_2FeGeS_4 is nonphase matchable within the range of wavelengths studied. The coherence length of Li_2FeGeS_4 is <20 μm. For nonphase-matchable NLO materials, the second-order NLO susceptibility, $\chi^{(2)}$, can typically be calculated using eq 4, based on the Kurtz method,[46] where I_S and I_R are experimentally measured SHG counts from the sample and the reference with l_R and l_S being their coherence lengths, respectively.

$$\chi_S^{(2)} = \chi_R^{(2)}(l_R/l_S)(I_S/I_R)^{1/2} \tag{4}$$

However, the $\chi^{(2)}$ value of Li_2FeGeS_4 was not calculated in this study since it undergoes strong absorption at wavelengths below 3 μm, which is approaching the limit of our experimental setup.

It is evident from Figure 8 that the SHG response of Li_2FeSnS_4 (d < 20 μm) is comparable to that of Li_2FeGeS_4. In addition to the strong absorption below 3 μm for Li_2FeSnS_4, the $\chi^{(2)}$ value has not been estimated since phase matchability could not be assessed due to the limited availability of particle sizes.

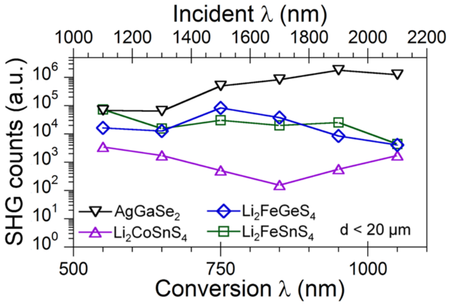

Figure 8. Broad-band SHG response as a function of incident and conversion wavelengths for Li_2CoSnS_4, Li_2FeGeS_4, and Li_2FeSnS_4 in comparison to a $AgGaSe_2$(MC) reference.

The SHG response of Li_2CoSnS_4 is similar to the ferrous DLSs, as shown in Figure 8. In contrast, phase matching is evident in Li_2CoSnS_4 for $\lambda \geq 2.1$ μm (Figure S4, Supporting Information); however, absorption effects may mask the coherence between the fundamental and the SHG beams. The $\chi^{(2)}$ values of new phase-matchable materials are ideally estimated by comparing a reference and sample in a range where the SHG responses of both are static and phase matchable. In this case, the static region for Li_2CoSnS_4 could not be established by acquiring SHG counts at $\lambda > 2.1$ μm due to the poor SHG efficiency at longer wavelengths caused by absorption of λ and λ_{SHG} (Figure 7a). Thus, the $\chi^{(2)}$ value for Li_2CoSnS_4 was not estimated.

Although SHG has been observed for Li_2FeGeS_4, Li_2FeSnS_4, and Li_2CoSnS_4, the responses within the measured range are weaker than the benchmark $AgGaSe_2$ (Figure 8) as well as the quaternary DLS Li_2CdGeS_4.[5,11,22] However, these three DLSs exhibit higher transparency further into the IR region that may persist into the THz regime. Considering that these transition metal-containing DLSs display appreciable SHG where absorption is clearly significant, Li_2FeGeS_4, Li_2FeSnS_4, and Li_2CoSnS_4 may display efficient NLO susceptibility further into the mid-IR (>5 μm) as well as the far-IR and even the THz ranges.

In addition to the wide region of optical clarity, Li_2MnGeS_4 exhibits significant SHG for a broad range of λ up to 4.05 μm. The behavior of Li_2MnGeS_4 is comparable to $AgGaSe_2$(MC) up to λ = 2.7 μm, at which point the SHG response of Li_2MnGeS_4 approaches a static region, as shown in Figure 9.

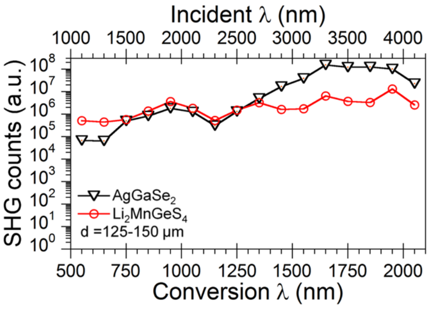

Figure 9. Broad-band SHG response as a function of incident and conversion wavelengths for Li_2MnGeS_4 in comparison to a $AgGaSe_2$(MC) reference.

The importance of collecting λ-dependent SHG response over a broad-band range for accurate NLO characterization is evident in the variance of the experimental SHG counts over the range of wavelengths for Li_2MnGeS_4 as well as the other DLSs. According to the particle-size dependence of the SHG response (Figure S2, Supporting Information), Li_2MnGeS_4 becomes phase matchable at λ = 1.6 μm (λ_{SHG} = 0.8 μm). Thus, the type-I phase-matchable region for Li_2MnGeS_4 is wider than the benchmark materials $ZnGeP_2$ ($\lambda \geq 2.0$ μm), $AgGaS_2$, and $AgGaSe_2$, as well as $LiInS_2$ and $LiInSe_2$ (Table 2).

The $\chi^{(2)}$ for phase-matchable materials can be estimated using eq 5, in which I_S and I_R are the SHG counts of the reference and sample with the same particle-size range at a λ region in which both are phase matchable and exhibit minimal absorption effects as well as static SHG behavior.

$$\chi_S^{(2)} = \chi_R^{(2)}(I_S/I_R)^{1/2} \tag{5}$$

Accordingly, the $\chi^{(2)}$ for Li_2MnGeS_4 is 15 ± 5 pm/V when a microcrystalline reference, $AgGaSe_2$(MC),[5] is used. It should be noted that $AgGaSe_2$(MC) exhibits a lower SHG response in comparison to $AgGaSe_2$(OQ)[5] that likely arises due to crystal defects (e.g., antisites, vacancies) within the powder. However, an improvement in SHG response may not always be observed when comparing a microcrystalline sample to an optical quality single crystal. Accordingly, the SHG response of Li_2MnGeS_4 may, or may not, be improved in optical quality, single crystals; thus, an upper bound in $\chi^{(2)}$ is reported which results from comparison to the $AgGaSe_2$(MC), while the lower bound,

Table 2. Comparison of Quaternary DLSs with Materials That Are Commercially Available NLO Materials for IR Applications[a]

compound	E_g (eV)	transparency window (μm)	transparency level	PM region (μm)	$\chi^{(2)}$ (pm/V)
Li_2FeGeS_4[b]	1.423(3)[19]	~3–25[b,c]	80%	NPM[b]	
Li_2FeSnS_4[b]	1.860(2)[19]	~3–25[b,c]	80%		
Li_2CoSnS_4[b]	2.421(3)[b]	~4–25[b,c]	65%	≥2.1[b]	
Li_2MnGeS_4[b]	3.069(3)[b]	0.60–25[b,c]	80%	≥1.6[b]	6.6[b,L], 15[b,U]
Li_2CdGeS_4	3.1544(8)[5]	0.50–23.5[5,c]	75%	≥1.5[5]	22.5,[b,L], 51[U,5]
$LiInS_2$[d]	3.6[6]	0.34–13.2[6,e]	0 level	≥2.3[8d]	6.8,[8b] 11.16,[8a] 13.8,[8d] 15[8c]
$LiInSe_2$[d]	2.86[7]	0.72–10.4[7,e]	$\alpha = 1\ cm^{-1}$	≥2.0[55]	17,[8d] 22[9]
α/β-Cu_2ZnSiS_4	~3.0/~3.2[38]	0.70–25[38,c]	75%	≥1.7[38]	6.6,[L] 15[U,38]
Cu_2CdSnS_4	0.92[38]	1.37–25[38,c]	60%	≥2.1[38]	27,[L] 62[U,38]
$AgGaS_2$[d]	2.6[2]	0.47–13[42,e]	0 level	≥1.8[56]	36[4]
$AgGaSe_2$[d]	1.8[2]	0.71–19[43,e]	0 level	≥3.1[56]	66[1]

[a] PM = phase matchable. [b] This work. [c] Obtained from optical diffuse reflectance and ATR spectroscopies on polycrystalline powders; NPM = nonphase matchable; L and U correspond to lower and upper bounds of the $\chi^{(2)}$ determined using $AgGaSe_2$(OQ) and $AgGaSe_2$(MC), respectively. [d] Commercially available. [e] Obtained from laser calorimetry measurements on single crystals.

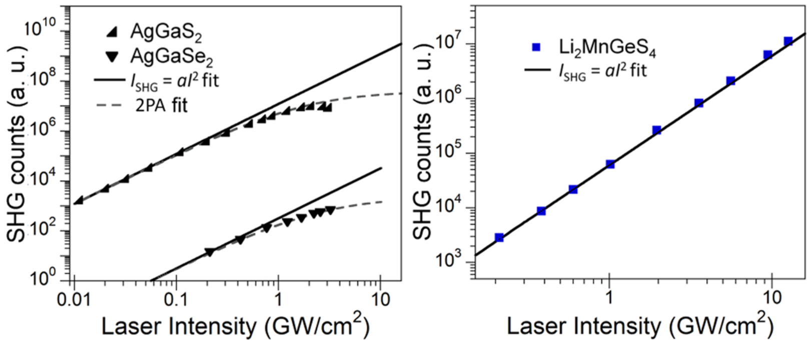

Figure 10. (Left) SHG power dependence of $AgGaS_2$(MC) and $AgGaSe_2$(MC) superimposed by square fits (solid black line) and 2PA fits (dashed gray line). (Right) SHG power dependence of Li_2MnGeS_4 superimposed by a square fit (solid black line).

6.6 ± 2 pm/V, is provided by comparison to the $AgGaSe_2$(OQ) reference.

The second-order NLO susceptibility of Li_2MnGeS_4 is within range of $LiInS_2$, while it is lower than that of $AgGaS_2$ and $AgGaSe_2$. These results are not surprising, considering that wider bandgaps are generally correlated with weaker NLO susceptibilities.[4] However, the $\chi^{(2)}$ of Li_2MnGeS_4 is well above that of the popular UV and visible NLO material KDP[47] with a wide bandgap of 7 eV and a $\chi^{(2)}$ value of 1 pm/V. Yet, wide bandgaps can also result in higher LDTs, which can be of chief value for practical considerations.

3.5. Laser Damage Threshold (LDT). Optimizing the threshold for laser-induced damage is key in the pursuit of new NLO crystals for laser applications, especially those that require high powers ($P_{avg} > 1$ kW)[48] because the LDT limits the maximum efficiency of optical processes in NLO materials and is often the ultimate restriction on system performance.[3b] Generally, laser-induced damage in defect-free crystals is initiated by the excitation of electrons to the conduction band from linear absorption and/or multiphoton absorption (MPA) processes. The LDT is highly dependent on the λ employed, as well as the laser pulse width (τ). When τ is longer than tens of picoseconds (ps), damage is induced by the heat that is transferred from the incident radiation to the conduction-band electrons when the heat is sufficient to melt or fracture the material;[49] thus, the laser damage is rate dependent on the thermal conduction throughout the lattice, which is affected by pulse duration. At shorter pulse durations (i.e., $\tau < 50$ ps), MPA processes dominate the mechanisms for laser-induced damage since the energy is absorbed by electrons much faster than it is transferred to the lattice.[49] Accordingly, MPA is expected to be the main mechanism for laser-induced damage reported here since $\tau = 30$ ps.

The phenomenon of MPA, in which the absorption of photons induces electronic excitation, occurs when $N\hbar\omega \geq E_g$, where $\hbar\omega$ is the energy of the incident radiation, N is the number of photons involved (i.e., $N = 2$ in two-photon absorption), and E_g is the bandgap energy. Thus, the probability of evading MPA at a given λ increases as the bandgap is widened since higher order MPA processes, with larger values of N, become increasingly improbable.[50] For example, $AgGaS_2$, with a bandgap of 2.6 eV,[2] undergoes two-photon absorption (2PA)[6] upon irradiation with $\lambda = 1.064$ μm ($\hbar\omega = 1.17$ eV) as shown in Figure 10. Although the bandgap of $AgGaS_2$ requires three-photon absorption (3PA) of the fundamental beam, we believe the presence of shallow impurities near the band edge (Figure S9, Supporting Information) allows for the simultaneous absorption of two photons. In another example, α/β-Cu_2ZnSiS_4 has a bandgap of ~3.1 eV,[51] and the observed laser damage is induced by 3PA[38] as expected.

In this study, the LDT of Li_2MnGeS_4 was evaluated and compared with that of the benchmark $AgGaS_2$ and $AgGaSe_2$ that were measured under the same conditions ($\tau = 30$ ps, $\lambda = 1.064$ μm). Measuring the LDTs using powder samples[5,52] is feasible since each crystallite has a diameter of 125−150 μm that is much larger than the λ of the incident laser; thus, each crystallite behaves as a macroscopic bulk material with similar MPA. The SHG counts, measured as a function of laser intensity, are expected to increase according to the square law shown in eq 6 when laser-induced damage is absent, as represented by solid black lines in Figure 10. The LDT is assigned as the point at which the observed SHG counts deviate from the expected SHG counts, as calculated using eq 6, where I is the fundamental intensity, I_{SHG} is the SHG intensity, and a is a proportionality constant that incorporates $\chi^{(2)}$.

$$I_{SHG} = aI^2 \tag{6}$$

Accordingly, the LDT of $AgGaSe_2$(MC and OQ) is ~0.2 GW/cm^2 as previously reported,[5,11] and $AgGaS_2$ exhibits a threshold of ~0.3−0.4 GW/cm^2. The observed SHG intensities for $AgGaS_2$(MC) were fit using eq 7, with β = 12 cm/GW, d = 125−150 μm, and a as determined by fitting the low-intensity portion that is free of MPA. Notably, the $AgGaS_2$(MC) sample, which is a microcrystalline powder sample obtained using conventional solid-state synthesis, has an LDT that is comparable with that of an optical quality single crystal of $AgGaS_2$(OQ) obtained from Gooch and Housego, as shown in Figure S7, Supporting Information. Further, $AgGaS_2$ undergoes photodarkening[53] that is likely due to a photoassisted reduction process of silver cations[54] (Figure S8, Supporting Information).

$$I_{SHG} = aI_{2PA}{}^2 \quad \text{with} \quad I_{2PA} = I/[1 + I\beta d] \tag{7}$$

Most remarkably, the wide-gap semiconductor Li_2MnGeS_4 (E_g = 3.069 eV) exhibits an outstanding LDT that is greater than 16 GW/cm^2 (Figure 10). The SHG counts for Li_2MnGeS_4 persist with the square law (eq 6), and the material exhibits neither the critical limitation of 2PA nor the expected 3PA up to a laser intensity of 16 GW/cm^2. Upon higher intensities, the fused-silica ampule that contains the sample is compromised.

Interestingly, the LDT of Li_2MnGeS_4 outshines even those of other I_2-II-IV-VI_4 DLSs with similar bandgaps ≥ 3 eV, while it is substantially higher than the narrow-gap quaternary DLSs (e.g., Cu_2CdSnS_4: E_g = 0.9 eV, LDT = 0.2 GW/cm^2). The α/β-Cu_2ZnSiS_4 sample exhibits a LDT of ~2 GW/cm^2,[38] that is attributed to 3PA and is an order of magnitude higher than the commercially available $AgGaSe_2$. On the other hand, Li_2CdGeS_4 (E_g ≈3.15 eV)[5] exhibits a slight fundamental depletion by 3PA at 5 GW/cm^2, but the absorption is saturable and the observed SHG counts resume the square law at I > 10 GW/cm^2.[22] While the behavior of Li_2CdGeS_4 is exceptional, the evidence that Li_2MnGeS_4 is entirely free of the MPA-induced damage is unprecedented.

The addition of Li_2MnGeS_4 to the two quaternary DLSs, α/β-Cu_2ZnSiS_4 and Li_2CdGeS_4 with E_g ≥ 3.0 eV that display substantially different laser-induced damage behavior, provides a unique opportunity to gain insight into the factors that influence the mechanisms of laser-induced damage. Generally, LDT can be understood in terms of an electron avalanche[57] where conduction-band electrons, which undergo laser-induced oscillation, transfer energy by scattering phonons.[49] As an electron is promoted from the valence band to the conduction band by laser irradiation, subsequent impact excites another electron. Essentially, the threshold for optical breakdown is determined by a delicate balance between the energy gained by the electrons and rates of energy loss.[49] Therefore, the three main factors that influence laser damage mechanisms for transparent (defect-free) materials are (1) the processes that initiate the avalanche, (2) the avalanche rates, which are governed by the effects of laser absorption on conduction-band electrons and, thus, conduction-electron momentum and energy scattering, and (3) the effects of significantly heating the lattice on the energy scattering rates.[49] As observed in Li-III-VI_2 materials, incorporating lithium into diamond-like chalcogenides provides increased frequencies of crystal lattice vibrations and Debye temperatures, thus yielding thermal conductivities that are greater than the Ag-based analogues.[58] In addition to the wide bandgap that lends to the extraordinary LDT observed for Li_2MnGeS_4, a favorable thermal conductivity is most probable. However, while thermal conductivity and bandgap are two of the important factors determining LDT in ideal materials, most samples are not perfect crystals.

LDT of real crystals will often be lower than that of perfect crystals due to defects and/or impurities. For very short pulse duration (~10 ps or shorter), LDT measurements more closely correspond to the intrinsic properties of the perfect material; however, in the longer pulse regime the LDT can be strongly influenced by defects and/or impurities.[49] Even if the laser intensity is not high enough to directly photoionize electrons, ionized impurity or defect states can provide the initial seed electrons for the electron avalanche.[59] For example, the generally accepted mechanism for laser-induced damage in KDP is attributed to defect states in the gap that essentially reduce the order of the MPA process needed for an electron to reach the conduction band.[60] As discussed above for $AgGaS_2$, the expected MPA process should be 3PA, while the LDT data indicate 2PA.

Our previous work and the results reported here show that the LDT for $AgGaS_2$ and $AgGaSe_2$, as ground optical-quality single crystals (OQ), were highly comparable to the LDT of the corresponding microcrystalline powders (MC).[5] This suggests that defects in the $AgGaS_2$ and $AgGaSe_2$ microcrystalline powders are not well avoided in the bulk single crystals. Since compound defects can act as trapping centers of free carriers leading to laser-induced damage as well as limit the transparency window of the material, it is important to perfect the crystal-growth procedure of candidate NLO materials since well-formed single crystals with minimal defects should allow for the maximum achievable threshold for laser-induced damage.[60] Therefore, future work will focus on growing sizable crystals of Li_2MnGeS_4 that could even outperform the polycrystalline sample reported here.

4. CONCLUSIONS

The optical clarity windows, regions of phase matchability, and second-order nonlinearity can be tuned in quaternary I_2-II-IV-VI_4 DLSs through compositional variations. The new Li_2CoSnS_4 DLS, with the wurtz-kesterite structure and a bandgap of 2.421 eV, is phase matchable at λ ≥ 2.1 μm. Significant SHG has been observed in Li_2-II-IV-S_4 DLSs that contain divalent transition metals, Co, Fe, and Mn, although Co- and Fe-containing compounds exhibit strong absorption within our observation range. Since the optical clarity windows of Li_2FeGeS_4, Li_2FeSnS_4, and Li_2CoSnS_4 extend at least to 25 μm, these DLSs may hold potential for laser applications that require long wavelengths.

Like Li_2CoSnS_4, the new Li_2MnGeS_4 DLS was accessed by employing the steadfast design strategy for DLSs. Li_2MnGeS_4, with a bandgap of 3.069 eV and the lithium cobalt (II) silicate structure, has a wide clarity window of 0.7−25 μm. It also has a phase-matching range (λ ≥ 1.6 μm) that exceeds the benchmark $AgGaSe_2$ and $AgGaS_2$, among others, and a $\chi^{(2)}$ value that is within the range of mature, commercially available NLO materials for use in the IR. Most notably, Li_2MnGeS_4 exhibits a LDT that is >16 GW/cm^2, which is more than 40×

higher than that of the benchmark NLO material $AgGaS_2$ and more than 8× higher than the close relative α/β-Cu_2ZnSiS_4. Li_2MnGeS_4 provides a unique and delicate balance between the energy absorbed by conduction-band electrons and energy lost through the lattice that circumvents MPA-induced damage under irradiation of a high-powered laser. Li_2MnGeS_4 is a new NLO material that holds great potential for high-power applications that require the generation of long-wavelength radiation up to the THz regime.

■ ASSOCIATED CONTENT

Ⓢ Supporting Information

Crystal structure details from single-crystal X-ray diffraction and Rietveld refinement using synchrotron X-ray powder diffraction data and conventional X-ray powder diffraction; SHG data. This material is available free of charge via the Internet at http://pubs.acs.org.

■ AUTHOR INFORMATION

Corresponding Author

*E-mail: aitkenj@duq.edu.

Author Contributions

The manuscript was written through contributions of all authors. All authors have given approval to the final version of the manuscript.

Notes

The authors declare no competing financial interest.

■ ACKNOWLEDGMENTS

This work was supported by the National Science Foundation, DMR-1201729. Use of the Advanced Photon Source, an Office of Science User Facility operated by the U.S. Department of Energy (DOE) Office of Science by Argonne National Laboratory, was supported by the U.S. DOE under Contract No. DE-AC02-05CH11357. Y.S.K. acknowledges support from the Basic Science Research Program (2014-010369) and Priority Research Center Program (2009-0093818) through the NRF of Korea funded by the Ministry of Education. Special thanks to several individuals of Gooch and Housego (Ohio) for useful discussions regarding laser-induced damage in NLO materials: Gary Catella (Director of Technology), Dr. Matthew Whittaker, and Dr. Carl Brunetta.

■ REFERENCES

(1) Ohmer, M. C.; Pandey, R. *MRS Bull.* **1998**, *23*, 16−22.

(2) Catellha, G. C.; Burlage, D. *MRS Bull.* **1998**, *23*, 28−36.

(3) (a) Schunemann, P. G. *Proc. SPIE* **2007**, *6455*, 64550R. (b) Kildal, H.; Iseler, G. W. *Appl. Opt.* **1976**, *15*, 3062−3065.

(4) Jackson, A. G.; Ohmer, M. C.; LeClair, S. R. *Infrared Phys. Technol.* **1997**, *38*, 233−244.

(5) Brant, J. A.; Clark, D. J.; Kim, Y. S.; Jang, J. I.; Zhang, J.-H.; Aitken, J. A. *Chem. Mater.* **2014**, *26*, 3045−3048.

(6) Isaenko, L.; Vasilyeva, I.; Yelisseyev, A.; Lobanov, S.; Malakhov, V.; Dovlitova, L.; Zondy, J. J.; Kavun, I. *J. Cryst. Growth* **2000**, *218*, 313−322.

(7) Isaenko, L.; Yelisseyev, A.; Lobanov, S.; Petrov, V.; Rotermund, F.; Slekys, G.; Zondy, J. J. *J. Appl. Phys.* **2002**, *91*, 9475−9480.

(8) (a) Knippels, G. M. H.; van der Meer, A. F. G.; MacLeod, A. M.; Yelisseyev, A.; Isaenko, L.; Lobanov, S.; Thénot, I.; Zondy, J. J. *Opt. Lett.* **2001**, *26*, 617−619. (b) Boyd, G. D.; Kasper, H. M.; MacFee, J. H. *J. Appl. Phys.* **1973**, *44*, 2809−2812. (c) Yelisseyev, A.; Isaenko, L.; Lovanov, S.; Zondy, J. J. *Advanced Solid State Lasers. In OSA Trends in Optics and Photonics Series*; Injeyan, H., Marshall, C., Eds.; Optical Society of America: Washington, D.C., 2000; Vol. 34, pp 561−569. (d) Chen, W.; Cousin, J.; Sigrist, M. W.; Gao, X.; Zondy, J. J.; Isaenko, L.; Yelisseyev, A.; Lobanov, S. In $LiInS_2$ and $LiInSe_2$: New nonlinear crystals for continuous-wave differency frequency generation in the mid-infrared. *19th Annual Meeting of the IEEE*; Laser and Electro-Optics Society: Montreal Canada, 2006; pp 88−89.

(9) Ebrahim-Zadeh, M. Mid-infrared optical parametric oscillators and applications. In *NATO Science for Peace and Security Series B: Physics and Biophysics. Mid-Infrared Coherent Sources and Applications*; Ebrahim-Zadeh, M., Gorokina, I. T., Eds.; Springer: Dordrecht, The Netherlands, 2008; pp 347−375.

(10) (a) Parthé, E. *Crystal Chemistry of Tetrahedral Structures*; Gordon and Breach Science Publishers, Inc.: New York, 1964. (b) Goryunova, N. A. *The Chemistry of Diamond-like Semiconductors*; Massachusetts Institute of Technology: Cambridge, MA, 1965.

(11) Aitken, J. A.; Brant, J. A.; Clark, D. J.; Kim, Y. S.; Jang, J. I. Impact of bandgap on infrared optical nonlinearity in novel quaternary chalcogenides: Cu_2CdSnS_4, a/b-Cu_2ZnSiS_4 and Li_2CdGeS_4. In *Nonlinear Optics: Fundamentals, Applications and Technological Advances*; Wilkins, F., Ed.; NOVA Scientific Publishers: New York, 2014.

(12) Pamplin, B. *Prog. Cryst. Growth Charact.* **1981**, *3*, 179−192.

(13) Zhao, B.-J.; Zhu, S.-F.; Yu, F.-L.; Li, H.-Y.; Gao, D.-Y.; Li, Z.-H. *Cryst. Res. Technol.* **1998**, *33*, 943−948.

(14) SAINT and SADABS are part of the Apex2 software package v2.1-4 Program for Data Collection and Reduction on Bruker AXS CCD Area Detector Systems. *Apex2 software package v2.1-4*; Bruker Analytical X-ray Systems, Inc., Madison, WI, 2005.

(15) Sheldrick, G. M. *Acta Crystallogr., Sect. A* **2007**, *A64*, 112−122.

(16) *SHELXTX-PC*, release 6.14; Bruker AXS: Madison, WI, 2007.

(17) (a) Larson, A. C.; Von Dreele, R. B. *Los Alamos National Laboratory Report LAUR*, 1994, pp 86−748. (b) Toby, B. H. *J. Appl. Crystallogr.* **2001**, *34*, 210−213.

(18) Brunetta, C. D.; Brant, J. A.; Rosmus, K. A.; Henline, K. M.; Karey, E.; MacNeil, J. H.; Aitken, J. A. *J. Alloys Compd.* **2013**, *574*, 495−503.

(19) Brant, J. A.; dela Cruz, C.; Yao, J.; Douvalis, A. P.; Bakas, T.; Sorescu, M.; Aitken, J. A. *Inorg. Chem.* **2014**, *53*, 12265−12274.

(20) McGowan, R. J. *Anal. Chem.* **1963**, *35*, 1664−1665.

(21) Jang, J. I.; Park, S.; Clark, D. J.; Saouma, F. O.; Lombadro, D.; Harrison, C. M.; Shim, B. *J. Opt. Soc. Am.* **2013**, *30*, 2292−2297.

(22) Jang, J. I.; Clark, D. J.; Brant, J. A.; Aitken, J. A.; Kim, Y. S. *Opt. Lett.* **2014**, *39*, 4579−4582.

(23) Yamaguchi, H.; Akatsuka, K.; Setoguchi, M.; Takaki, Y. *Acta Crystallogr.* **1979**, *B35*, 2680−2682.

(24) Brunetta, C. D.; Minsterman, W. C.; Lake, C. H.; Aitken, J. A. *J. Solid State Chem.* **2012**, *187*, 177−185.

(25) (a) Parthé, E.; Yvon, K.; Deitch, R. H. *Acta Crystallogr.* **1969**, *25*, 1164−1174. (b) Nitsche, R.; Sargent, D. F.; Wild, P. *J. Cryst. Growth* **1967**, *1*, 52−53.

(26) Ilyukhin, V. V.; Nikitin, A. V.; Belov, N. V. *Sov. Phys. Dokl.* **1966**, *11*, 1035−1038.

(27) Brunetta, C. D.; Karuppannan, B.; Rosmus, K. A.; Aitken, J. A. *J. Alloys Compd.* **2012**, *516*, 65−72.

(28) Lekse, J. W.; Leverett, B. M.; Lake, C. H.; Aitken, J. A. *J. Solid State Chem.* **2008**, *181*, 3217−3222.

(29) Lekse, J. W.; Moreau, M. A.; McNerny, K. L.; Yeon, J.; Halasyamani, P. S.; Aitken, J. A. *Inorg. Chem.* **2009**, *48*, 7516−7518.

(30) Boultif, A.; Louer, D. J. *Appl. Crystallogr.* **2004**, *37*, 724−731.

(31) Abrahams, S. C. *Acta Crystallogr.* **1955**, *8*, 661−671.

(32) Hardy, A.; Perez, G.; Serment, J. *Bull Soc. Chim. Fr.* **1965**, 2638−2640.

(33) Lundqvist, D.; Westgren, A. *Z. Anorg. Allg. Chem.* **1938**, *239*, 85−88.

(34) (a) Urbach, F. *Phys. Rev.* **1953**, *92*, 1324. (b) Pankove, J. I. *Optical properties in Semiconductors*; Dover Publications: New York, 1971.

(35) (a) Bai, L.; Lin, S. S.; Wang, Z. Z.; Chen, C. T. *J. Appl. Phys.* **2008**, *103*, 083111. (b) Li, L.-H.; Li, J.-Q.; Wu, L.-M. *J. Solid State Chem.* **2008**, *181*, 2462−2468.

DOI: 10.1021/ic502981r
Inorg. Chem. 2015, 54, 2809−2819

(36) Kosobutsky, A. V.; Basalaev, Y. M. *J. Phys. Chem. Solids* **2010**, *71*, 854−861.
(37) Li, Y.; Fan, W.; Sun, H.; Cheng, X.; Li, P.; Zhao, X. *J. Phys.: Condens. Matter* **2011**, *23* (225401), 1−11.
(38) Rosmus, K. A.; Brant, J. A.; Wisneski, S. D.; Clark, D. J.; Kim, Y. S.; Jang, J. I.; Brunetta, C. D.; Zhang, J.-H.; Srnec, M. N.; Aitken, J. A. *Inorg. Chem.* **2014**, *53*, 7809−7811.
(39) Platonov, A. N.; Marfunin, A. S. *Geochem. Int.* **1968**, 245−259.
(40) Chung, I.; Malliakas, C. D.; Jang, J. I.; Canlas, C. G.; Weliky, D. P.; Kanatzidis, M. G. *J. Am. Chem. Soc.* **2007**, *129*, 14996−15006.
(41) Chung, I.; Song, J. H.; Jang, J. I.; Freeman, A. J.; Kanatzidis, M. G. *J. Solid State Chem.* **2010**, *195*, 161−165.
(42) Badikov, V. V.; Pivovarov, O. N.; Skokov, Y. V.; Skrebneva, O. V.; Trotsenko, N. K. *Sov. J. Quantum Electron.* **1975**, *5*, 597−598; *Kvant. Elektron* **1975**, *2*, 1090−1092 transl. from.
(43) Barnes, N. P.; Gettemy, D. J.; Hietanen, J. R.; Iannini, R. A. *Appl. Opt.* **1989**, *28*, 5162−5168.
(44) Vodopyanov, K. L. *J. Opt. Soc. Am. B* **1993**, *10*, 1723−1729.
(45) Ok, K. M.; Chi, E. O.; Halasyamani, P. S. *Chem. Soc. Rev.* **2006**, *35*, 710−717.
(46) (a) Kurtz, S. K.; Perry, T. T. *J. Appl. Phys.* **1968**, *39*, 3798−3813. (b) Jang, J. I.; Chung, I.; Ketterson, J. B.; Kanatzidis, M. G. Nonlinear optical chalcogenide fibers and films of $APSe_6$ (A = K, Rb). In *New Developments in Photon and Materials Research*; Jang, J. I., Ed.; NOVA Scientific Publishers: New York, 2013.
(47) Villars, P.; Calvert, L. D. *Pearson's Handbook of Crystallographic Data for Intermetallic Phases*; American Society for Metals: Metals Park, OH, 1985; Vols. *I*−*-III*.
(48) Hopkins, F. K. *Opt. Photonics News* **1998**, *9*, 32−38.
(49) Stuart, B. C.; Feit, M. D.; Herman, S.; Rubenchik, A. M.; Shore, B. W.; Perry, M. D. *Phys. Rev. B* **1996**, *53*, 1749−1761.
(50) Klein, C. A.; Miller, R. P.; DeSalvo, R. J. *Proc. SPIE* **1994**, *2114*, 25−35.
(51) Rosmus, K. A.; Brunetta, C. D.; Srnec, M. N.; Karuppannan, B.; Aitken, J. A. *Z. Anorg. Allg. Chem.* **2012**, *638*, 2578−2584.
(52) Wu, Q.; Meng, X.; Zhong, C.; Chen, X.; QIn, J. *J. Am. Chem. Soc.* **2014**, *136*, 5683−5686.
(53) Paschotta, R. Photodarkening, retrieved Jan 19, 2015. http://www.rp-photonics.com/photodarkening.html.
(54) Kim, Y.; Seo, I.; Martin, S. W.; Baek, J.; Halasyamani, P. S.; Arumugam, N.; Steinfink, H. *Chem. Mater.* **2008**, *20*, 6048−6052.
(55) Petrov, V.; Zondy, J.-J.; Bidault, O.; Isaenko, L.; Vedenyapin, V.; Yelisseyev, A.; Chen, W.; Tyazhev, A.; Lobanov, S.; Marchev, G.; Kolker, D. *J. Opt. Soc. Am. B* **2010**, *27*, 1902−1927.
(56) Bordui, P. F.; Fejer, M. M. *Annu. Rev. Mater. Sci.* **1993**, *23*, 321−379.
(57) (a) Bloembergen, N. *IEEE J. Quantum Electron.* **1974**, *QE-10*, 375−386. (b) Holway, L. H., Jr.; Fradin, D. W. *J. Appl. Phys.* **1975**, *46*, 279−291. (c) Sparks, M.; Mills, D. L.; Warren, R.; Holstein, T.; Maradudin, A. A.; Sham, L. J.; Loh, E., Jr.; King, D. F. *Phys. Rev. B* **1981**, *24*, 3519−3536. (d) Manakov, A. A.; Prokhorov, A. M. *Usp. Fiz. Nauk* **1986**, *148*, 179−211;(f) *Sov. Phys. Usp.* **1986**, *29*, 104. trans. (e) Jones, S. C.; Braunlich, P.; Casper, R. T.; Shen, X.-A.; Kelly, P. *Opt. Eng.* **1989**, *28*, 1039−1068.
(58) Ma, T.; Sun, L.; Xu, C.; Chen, Y. *J. Alloys Compd.* **2011**, *509*, 9733−9741.
(59) Schaffer, C. B.; Brodeur, A.; Mazur, E. *Meas. Sci. Technol.* **2001**, *12*, 1784−1794.
(60) Wang, K.; Fang, C.; Zhang, J.; Sun, X.; Wang, S.; Gu, Q.; Zhao, X.; Wang, B. *J. Cryst. Growth* **2006**, *287*, 478−482.